

MIT Open Access Articles

Quantification of labile heme in live malaria parasites using a genetically encoded biosensor

The MIT Faculty has made this article openly available. **Please share** how this access benefits you. Your story matters.

Citation: Abshire, James R. et al. "Quantification of Labile Heme in Live Malaria Parasites Using a Genetically Encoded Biosensor." Proceedings of the National Academy of Sciences 114, 11 (March 2017): E2068–E2076 © 2017 National Academy of Sciences

As Published: <http://dx.doi.org/10.1073/pnas.1615195114>

Publisher: National Academy of Sciences (U.S.)

Persistent URL: <http://hdl.handle.net/1721.1/111215>

Version: Final published version: final published article, as it appeared in a journal, conference proceedings, or other formally published context

Terms of Use: Article is made available in accordance with the publisher's policy and may be subject to US copyright law. Please refer to the publisher's site for terms of use.



Quantification of labile heme in live malaria parasites using a genetically encoded biosensor

James R. Abshire^a, Christopher J. Rowlands^a, Suresh M. Ganesan^a, Peter T. C. So^{a,b}, and Jacquin C. Niles^{a,1}

^aDepartment of Biological Engineering, Massachusetts Institute of Technology, Cambridge, MA 02139; and ^bDepartment of Mechanical Engineering, Massachusetts Institute of Technology, Cambridge, MA 02139

Edited by Thomas E. Wellem, National Institutes of Health, Bethesda, MD, and approved January 25, 2017 (received for review September 11, 2016)

Heme is ubiquitous, yet relatively little is known about the maintenance of labile pools of this cofactor, which likely ensures its timely bioavailability for proper cellular function. Quantitative analysis of labile heme is of fundamental importance to understanding how nature preserves access to the diverse chemistry heme enables, while minimizing cellular damage caused by its redox activity. Here, we have developed and characterized a protein-based sensor that undergoes fluorescence quenching upon heme binding. By genetically encoding this sensor in the human malarial parasite, *Plasmodium falciparum*, we have quantified cytosolic labile heme levels in intact, blood-stage parasites. Our findings indicate that a labile heme pool ($\sim 1.6 \mu\text{M}$) is stably maintained throughout parasite development within red blood cells, even during a period coincident with extensive hemoglobin degradation by the parasite. We also find that the heme-binding antimalarial drug chloroquine specifically increases labile cytosolic heme, indicative of dysregulation of this homeostatic pool that may be a relevant component of the antimalarial activity of this compound class. We propose that use of this technology under various environmental perturbations in *P. falciparum* can yield quantitative insights into fundamental heme biology.

heme | heme sensor | genetically encoded biosensor | malaria | *Plasmodium falciparum*

Heme is a cofactor of central importance across biology and plays vital roles in diverse processes including energy production, oxygen transport, gas sensing, signaling (1), and catalysis (2). Its inherently high and tunable redox potential together with its diverse ligand-binding properties make it an extremely versatile cofactor suited to a broad range of chemistries. Free heme redox cycles in the aerobic and reducing cellular environment, which can induce potentially cytotoxic oxidative stress. To minimize this, both heme levels and reactivity are restricted in several ways, including sequestering it into protein scaffolds that determine the selectivity and specificity of its chemistry, degradation, export, and inactivation by physical processes such as crystallization (2–4). Cells maintain labile pools of critical cofactors to meet rapidly changing metabolic demands. Such pools for transition metal cofactors including iron and zinc, which can also be cytotoxic, have been quantitatively defined using an extensive toolkit (5, 6). However, similar and generally accessible tools for studying labile heme pools in live cells have not been widely available, and this has precluded achieving a detailed and quantitative understanding of cellular heme pool composition and dynamics under both physiologic and perturbed states.

We have been particularly interested in characterizing labile heme pools in the human malarial parasite, *Plasmodium falciparum*. This pathogen is a major cause of the 214 million cases and 438,000 deaths per year due to malaria (7). Several aspects of heme metabolism in *P. falciparum* are counterintuitive, and its exquisite sensitivity to heme-interacting antimalarial drugs suggests a critical and finely balanced role for heme in its biology. During development within red blood cells (RBCs), *P. falciparum* takes up and digests between 30 and 70% of the hemoglobin in a specialized subcellular digestive vacuole (DV) to release peptides and heme (8–11). The majority of this heme is converted

into crystalline hemozoin, which is relatively redox-inert (8, 11). Although the extent of hemoglobin digestion and heme crystallization is relatively lower in early-stage parasites (rings), this progressively increases as parasites develop through mid (trophozoite) and late (schizont) stages.

It is presently unknown whether hemoglobin-derived heme is quantitatively converted into hemozoin and exclusively confined to the DV, or whether it escapes the DV to accumulate in other compartments such as the parasite cytoplasm during normal development. Such a heme pool may be important for meeting metabolic needs, signaling to coordinate DV biochemistry with cytosolic and nuclear processes, or simply a consequence of obligate hemoglobin degradation by the parasite. Along these lines, despite liberating large quantities of heme from hemoglobin that should be more than adequate to meet the parasite's needs, the *P. falciparum* genome encodes a complete heme biosynthetic pathway that appears to be active in blood-stage parasites (12–14). Nevertheless, de novo heme biosynthesis is dispensable during the blood-stage infection, as the genes encoding δ -aminolevulinic acid synthase (ALAS) and ferrochelatase that are required for de novo heme biosynthesis can be deleted without observable defects in parasite growth (13, 15). Based on these studies, it has been suggested that hemoglobin-derived heme may escape the DV to completely meet the parasite's heme requirement. However, the physiologic levels of bioavailable heme, irrespective of its source, are yet to be defined.

Further highlighting the importance of heme biochemistry in the parasite is the potent antimalarial activity of chloroquine, an exemplar of the heme-binding 4-aminoquinoline drug class.

Significance

Malaria parasites degrade substantial quantities of hemoglobin to release heme within a specialized digestive vacuole. Most of this heme is sequestered in an inert crystal. However, the concentration of bioavailable, labile heme in the parasite's cytosol was unknown. We developed a biosensor to provide the first quantitative insights into labile heme concentrations in malaria parasites. We find that $\sim 1.6 \mu\text{M}$ labile cytosolic heme is maintained, including during a period coincident with intense hemoglobin degradation. The heme-binding antimalarial drug, chloroquine, which interferes with heme crystallization, specifically induces an increase in labile heme. The ability to quantify labile heme in malaria parasites opens opportunities for better understanding heme homeostasis, signaling, and metabolism, and its association with antimalarial potency.

Author contributions: J.R.A., C.J.R., and J.C.N. designed research; J.R.A., C.J.R., and S.M.G. performed research; J.R.A. and C.J.R. contributed new reagents/analytic tools; J.R.A., C.J.R., P.T.C.S., and J.C.N. analyzed data; and J.R.A., C.J.R., and J.C.N. wrote the paper.

The authors declare no conflict of interest.

This article is a PNAS Direct Submission.

Freely available online through the PNAS open access option.

¹To whom correspondence should be addressed. Email: jcniles@mit.edu.

This article contains supporting information online at www.pnas.org/lookup/suppl/doi:10.1073/pnas.1615195114/-DCSupplemental.

These compounds accumulate within the parasite's DV to disrupt hemozoin formation, and the noncrystallized heme is proposed to escape the DV to cause toxicity (11). Consistent with this, electron spectroscopic imaging of fixed, chloroquine-treated parasites revealed a qualitative increase in cytosolic iron content, suggestive of increased heme content in the parasite's cytoplasm (16). However, heme can be degraded in a glutathione-dependent manner to release iron (17), the extent of which cannot be inferred from the data. Fractionation studies on chloroquine-treated parasites also support an increase in labile heme, but its precise subcellular distribution cannot be inferred (16). Thus, direct and quantitative evidence of cytosolic heme accumulation in chloroquine-treated parasites is still lacking, despite the central importance of this knowledge to understanding the mechanism of action of arguably the most successful antimalarial drug class used to date.

Here, we have addressed the fundamental challenge of directly quantifying labile heme in live cells by systematically developing, validating, and optimizing a genetically encoded fluorescence-based heme biosensor. Using the optimized biosensor, we demonstrate that *P. falciparum* maintains a labile cytosolic heme pool throughout its blood-stage development. Furthermore, we directly show that disrupting heme sequestration in the DV using a heme-binding antimalarial drug causes a significant increase in the concentration of cytosolic labile heme, thus directly linking chloroquine to cell-wide heme perturbation. We believe that this biosensor will be broadly useful for directly interrogating heme biology in *P. falciparum* and in other organisms.

Results

Design and Characterization of a Quenched Fluorescence Heme Biosensor. We initially set out to design a FRET-based heme sensor constructed analogously to some previously described

small-molecule biosensors, in which an analyte-sensing domain is flanked by a donor–acceptor pair (18). Our data indicated, however, that although heme sensors of this design exhibit FRET in the *apo*-state, heme binding quenched energy transfer from the donor. In our proof-of-concept sensor, we selected enhanced cyan and yellow fluorescent proteins (ECFP and EYFP), respectively, as the donor and acceptor, and *P. falciparum* histidine rich protein 2 (*Pf*HRP2) without its signal peptide as the heme-binding domain (Fig. 1A). We chose *Pf*HRP2 as the heme sensor domain as this protein was previously shown to noncooperatively bind ~15–18 heme molecules/monomer with modest (~0.3 μ M) apparent affinity (19, 20). This modest affinity for heme minimizes the potential for a sensor based on this protein to act as a heme sink in cells, especially if a minimal length *Pf*HRP2 fragment with reduced heme-binding stoichiometry can be defined (see below). *Pf*HRP2 is nonessential to the parasite and is predominantly trafficked to the infected RBC cytosol or the parasite's DV to a lesser extent (20, 21). Thus, *Pf*HRP2 does not play an essential role in the parasite's cytosol, apicoplast, or mitochondrial compartments, and expressing it (or fusions thereof) in these compartments should not interfere with its physiologic role(s).

Therefore, we created a test construct (CHY) in which *Pf*HRP2 was flanked by ECFP and EYFP. We also made a control construct (CSY)—which should exhibit heme-independent and constitutive FRET (22)—by substituting the *Pf*HRP2 sensor domain for a (Gly₄Ser)₃ peptide spacer.

We recombinantly expressed and purified CHY and CSY to characterize their biochemical and spectroscopic properties *in vitro* (Fig. S1). We first tested whether flanking *Pf*HRP2 by ECFP and EYFP interfered with its heme-binding properties. Heme binding to *Pf*HRP2 occurs via bis-histidyl ligation, which causes a shift in the heme Soret peak absorbance from ~396 to 416 nm. Monitoring this change by UV-visible spectroscopy while titrating heme levels facilitates determination of heme-binding

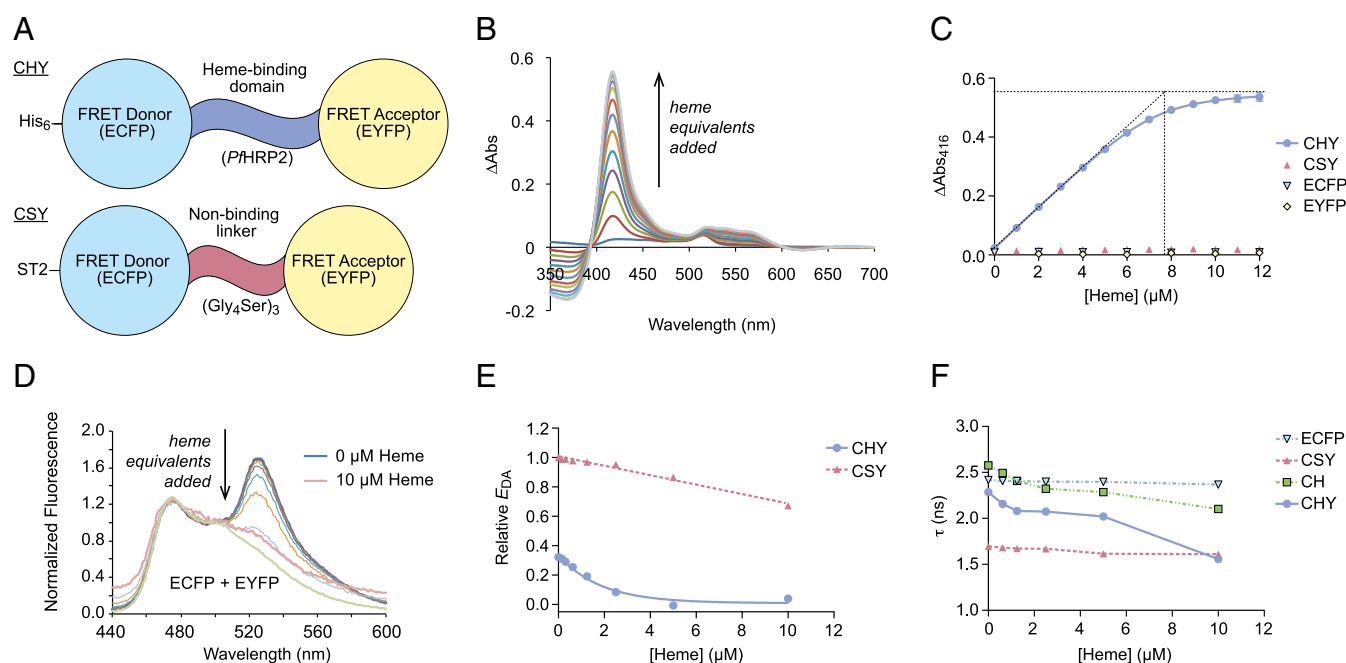


Fig. 1. Design and characterization of the initial heme biosensor. (A) Schematic of CHY heme sensor and CSY nonsensing control. (B) Representative difference absorption spectrum of the CHY during titration with heme. (C) Heme-binding isotherms based on Δ Abs_{416nm} Soret peak absorbance for CHY (blue circles), CSY (red triangles), ECFP (cyan inverted triangles), and EYFP (yellow diamonds). The solid line indicates the best fit for the CHY data using a single-site binding model and accounting for ligand depletion. (D) Normalized fluorescence intensity spectra for CHY titrated with heme. (E) Normalized EDA for CHY (blue circles) and CSY (red triangles) fitted to a single-exponential decay model (blue solid line) and a line (red dashed line), respectively. (F) Dependence of ECFP fluorescence lifetime on heme concentration for the CHY (blue circles), CH (green squares), ECFP (cyan inverted triangles), and CSY (red triangles) constructs.

stoichiometry and apparent heme-binding affinity to *Pf*HRP2 (19, 23). Heme titrations with CHY produced the expected increase in absorbance at 416 nm, consistent with binding to *Pf*HRP2 (Fig. 1*B*). Analysis of these data by breakpoint detection and fitting to a ligand binding with depletion model (23) (Fig. 1*C*), respectively, revealed that CHY bound ~15 heme equivalents per monomer with an apparent K_D value of ~0.25 μ M. These data are in good agreement with previously published data obtained for recombinant *Pf*HRP2 (19, 20), indicating that fusion to ECFP and EYFP did not significantly alter its heme-binding properties. Furthermore, no heme binding to ECFP, EYFP, and CSY could be detected in similar heme titration experiments (Fig. 1*C*), indicating that *Pf*HRP2 accounts for all spectroscopically detectable heme binding to CHY.

Next, we assessed the FRET properties of CHY and CSY. Based on earlier studies with model FRET constructs of the design CFP-linker-YFP (22), we expected that CHY and CSY would produce efficient FRET in the absence of heme. Indeed, for both CHY and CSY, direct ECFP excitation at 420 nm produced emission spectra with maxima at 475 nm (ECFP emission) and 525 nm (EYFP emission) (Fig. 1*D*). The latter emission peak is indicative of FRET between the ECFP donor and EYFP acceptor. Further supporting this interpretation, when a 1:1 mixture of ECFP and EYFP was excited at 420 nm, only the characteristic ECFP emission spectrum with a maximum at 475 nm but no emission maximum at 525 nm was detected. This indicates that interaction of the donor and acceptor pair in *trans* is insufficient to produce the observed FRET. We then titrated CHY and CSY with heme while exciting at 420 nm. For CHY, detected YFP emission sharply decreased upon adding heme, and at 10 μ M heme, no EYFP emission was detectable (Fig. 1*D* and *E*). For CSY, only a modest decrease in EYFP emission was detected upon titrating heme (Fig. 1*D* and *E*). These data are consistent with CHY functioning as a “turn-off” sensor upon heme binding to the *Pf*HRP2 domain.

To gain insight into why CHY functioned as a turn-off heme sensor, we compared heme-dependent ECFP fluorescence lifetimes (Fig. S2) for ECFP, CSY, CHY, and an ECFP-*Pf*HRP2 fusion (CH) (Fig. 1*F*). ECFP fluorescence lifetime in both CHY and CH decreased upon titrating heme but was unchanged for ECFP and CSY. With no heme bound, *Pf*HRP2 exists as a random coil, but upon binding heme undergoes a conformational change to adopt partial 3_{10} -helical structure (19). A transition from random coil to a more rigid helical structure that physically separates the donor-acceptor pair could reduce energy transfer from ECFP to EYFP. However, this would be accompanied by an increase in ECFP lifetime during heme titrations, rather than the observed decrease. This indicated that our sensor did not behave like a classical FRET sensor. Heme-dependent changes in ECFP fluorescence lifetime in the CH and CHY constructs could be due to dynamic or static quenching of the emitted ECFP or EYFP fluorescence by heme bound to *Pf*HRP2. This mechanism is consistent with the decrease in ECFP lifetime observed in our experiments upon heme binding, and is supported by an earlier observation showing that irreversible heme binding to a cytochrome *b*₅₆₂-GFP fusion strongly quenched GFP fluorescence (24).

Optimization of Initial Heme Biosensor Design. Having established that inserting *Pf*HRP2 between ECFP and EYFP produces a heme sensor, we sought to improve this design by defining a minimal *Pf*HRP2 fragment that preserved heme binding while maximizing heme-dependent changes in energy transfer. Based on model studies, these parameters may be simultaneously optimized by selecting shorter linkers between donor and acceptor fluorophores (22). We also reasoned that reducing the heme-binding capacity of our sensor together with its inherently modest

binding affinity would minimize the potential for the sensor to act as a heme sink.

We made a minilibrary of *Pf*HRP2 fragments containing variable numbers of heme-binding motifs (25, 26) and cloned these between ECFP and EYFP to create several sensors. These are annotated as CH_{*x*}Y, where *x* is the number of *Pf*HRP2-derived amino acids comprising the heme binding domain (Fig. 2*A* and Fig. S3). We recombinantly expressed and purified these constructs, and determined that all bound heme with apparent affinities similar to full-length CHY and stoichiometries that were directly proportional to the length of the heme-binding domain (Fig. 2*B* and Fig. S4). In addition, the heme-sensing dynamic range was improved with shorter heme-binding domains (Fig. 2*C*). Because the *apo*-sensor exhibited FRET, but energy transfer from ECFP to EYFP decreased due to a quenching mechanism rather than a change in the spatial relationship between the donor and acceptor pair induced by heme binding (i.e., classical FRET), we defined an operational metric, E_{DA} , to reflect the effective efficiency of donor-to-acceptor energy transfer. We calculated this identically to E_{FRET} (27) but use the E_{DA} nomenclature to specify that the original FRET signal from the *apo*-sensor changes in response to heme binding through quenching of donor energy transfer. Using this metric, we determined that E_{DA} for all sensors decreased upon heme binding, with half-maximal values between 2 and 6 μ M heme (Figs. S5 and S6). Sensors with shorter *Pf*HRP2 sensing domain fragments exhibited greater E_{DA} dynamic range (Fig. 2*C* and Fig. S5).

We selected the CH₄₉Y sensor construct for further development due to its improved dynamic range over CHY and retained responsiveness to heme. To preserve the option of using EYFP fluorescence as a direct readout of heme binding to the sensor, which would facilitate data collection using commonly available epifluorescence rather than more specialized fluorescence lifetime imaging microscopes, we implemented a strategy to correct for heme-independent environmental effects on our donor-acceptor fluorophores. For example, previous studies have shown that EYFP fluorescence is sensitive to chloride ions (28), the cytosolic concentration of which may be unknown in different biological contexts. To achieve this, we used CSY as a normalization control for any heme-independent environmental effects on the fluorophores. We evaluated the robustness of this approach by determining the efficiency of energy transfer for CH₄₉Y (E_{DA}^{CH49Y}) and CSY (E_{DA}^{CSY}) in the absence and presence of 120 mM potassium chloride (Fig. S7*A* and *B*). Our data showed that this normalization approach effectively corrected for chloride-induced effects such that over a broad range of heme concentrations, $E_{DA}^{CH49Y}/E_{DA}^{CSY}$ at 0 and 120 mM KCl are indistinguishable (Fig. S7*C*). We used our *in vitro* data for E_{DA}^{CH49Y} and E_{DA}^{CSY} (Fig. 2*D*) to establish a calibration curve defining the relationship between normalized efficiency of CH₄₉Y energy transfer ($E_{DA}^{CH49Y}/E_{DA}^{CSY}$) and heme concentration (Fig. 2*E* and *Materials and Methods*).

Measuring Labile Cytosolic Heme in Live *P. falciparum* Parasites. We focused next on using our heme sensor to quantify cytosolic labile heme concentrations in *P. falciparum* using fluorescence microscopy imaging. First, we sought to establish that E_{DA} determined using fluorimetry and fluorescence imaging correlated well with each other, as this would facilitate external calibration curves (Fig. 2*E*) to be used for determining intracellular heme concentrations. To test this, we encapsulated solutions of purified sensor and control proteins into giant multilamellar vesicles (GMVs) and measured E_{DA} by fluorescence microscopy. In parallel, we determined E_{DA} for the same solutions using fluorimetry. Although GMVs emitted fluorescence consistent with the loaded proteins, only those containing CH₄₉Y or CSY exhibited significant E_{DA} (Fig. 3*A*). These data showed that the mean apparent E_{DA} values determined by imaging and fluorimetry agreed

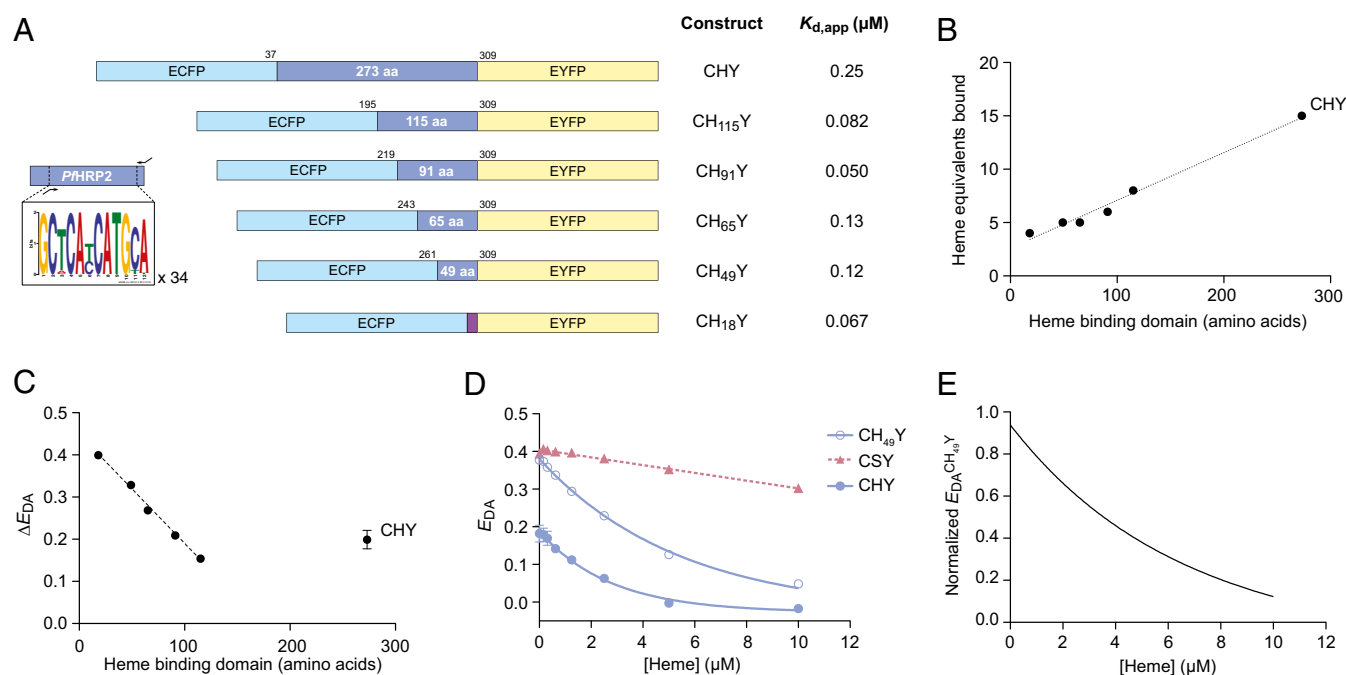


Fig. 2. Optimization to improve heme biosensor dynamic range. (A) Schematic of the minilibrary of *PfHRP2* fragments (shown in blue) evaluated for improved energy transfer properties. The fragment length (in amino acids) and the amino acid coordinates for mapping each fragment onto full-length *PfHRP2* are indicated. Apparent dissociation constants ($K_{d,app}$) are also shown. (B) Heme-binding stoichiometry varies linearly with length of the *PfHRP2*-derived heme-binding domain. (C) Dependence of ΔE_{DA} [$=E_{DA}$ (no heme) $- E_{DA}$ (saturating heme)] on length of the *PfHRP2*-derived heme-binding domain. (D) E_{DA} dependence on heme concentration for optimized CH₄₉Y (blue hollow circles) relative to the original sensor CHY (filled blue circles) and CSY (red triangles). (E) Calibration curve relating normalized $E_{DA}^{CH_{49}Y}$ to heme concentration (Materials and Methods).

closely (Fig. 3B). Furthermore, by encapsulating the *apo*-sensor minilibrary having a range of different E_{DA} values (Fig. 2A–C), we determined that fluorescence imaging microscopy and fluorimetry yield highly correlated outcomes (Fig. 3C). Altogether, these data validated that E_{DA} determined by microscopy can be accurately translated into heme concentrations based on fluorimetrically determined calibration data.

Next, we created clonal parasite lines on an NF54^{attB} (29) background separately expressing the CH₄₉Y sensor and CSY control. We also created several spectral control cell lines expressing ECFP, EYFP, and both ECFP and EYFP as individual proteins for calibrating E_{DA} calculations. All lines homogeneously expressed the respective proteins within the parasite's cytosol as determined by epifluorescence microscopy (Fig. 4A) and flow cytometry (Fig. S8). We also confirmed by Western blot that both CH₄₉Y and CSY are expressed as full-length proteins, thus eliminating proteolysis or premature translational termination as potential confounding factors in our subsequent data analyses (Fig. 4B).

During initial studies, we observed that normalized $E_{DA}^{CH_{49}Y}$ for normally developing late-stage parasites [0.69; 95% confidence interval (CI): 0.65–0.72] was significantly lower than in heme-free GMVs (0.93; 95% CI: 0.91–0.95) (Fig. 3B). As expected, parasites expressing ECFP and EYFP as individual proteins exhibited a mean E_{DA} close to zero (95% CI: -0.013 to 0.0022). As both CH₄₉Y and CSY are expressed as full-length proteins (Fig. 4B), degradation that preferentially reduces energy transfer for CH₄₉Y relative to that of CSY would not account for this observation. Based on our calibration data (Figs. 2E and 3C) and 15 independent experiments, we observed an average normalized $E_{DA}^{CH_{49}Y} = 0.71$ (95% CI: 0.710–0.716) in late-stage parasites, consistent with a 1.6 μ M cytosolic labile heme pool (95% CI: 1.56–1.61 μ M).

We then sought to understand the dynamics of this labile heme pool over the course of the 48-h *P. falciparum* intra-erythrocytic developmental cycle (IDC). As previously discussed, hemoglobin degradation is a potential source of a labile cytosolic heme in the parasite (13, 30). As the quantity of hemoglobin degraded significantly increases during progression through the IDC, we wanted to determine whether labile cytosolic heme levels would similarly rise or whether these would be maintained at relatively constant levels throughout. Using highly synchronous parasite cultures, we monitored normalized $E_{DA}^{CH_{49}Y}$ in ring-stage [4 h postinvasion (hpi)], trophozoite-stage (16 and 28 hpi), and schizont-stage (38 hpi) parasites. Intriguingly, the metabolic changes associated with progression through the IDC appear to have minimal effects on the labile cytosolic heme pool (Fig. 4D). This suggests that, despite increased hemoglobin degradation in the DV of trophozoite and schizont-stage parasites, labile heme levels in the cytosol are maintained within narrow limits during parasite development.

Quantitative Analysis of Perturbed Heme Homeostasis by Heme-Interacting Antimalarials. We next used our heme sensor to gain direct insight into a proposed mechanism of antimalarial drug action. Heme-interacting antimalarial drugs, such as chloroquine, comprise one of the most successful classes, yet fundamental aspects of their mechanism of action remain unknown. Indeed, a more detailed understanding of these mechanisms could potentially be exploited for developing the next generation of antimalarial drugs that are not immediately compromised due to cross-resistance (31). Heme-binding antimalarial drugs have been proposed to interfere with detoxification of hemoglobin-derived heme by inhibiting its crystallization into hemozoin, thereby increasing labile heme concentrations to toxic levels (11). However, the effects of inhibiting hemozoin formation in the DV on heme levels in other parasite compartments have been a challenging

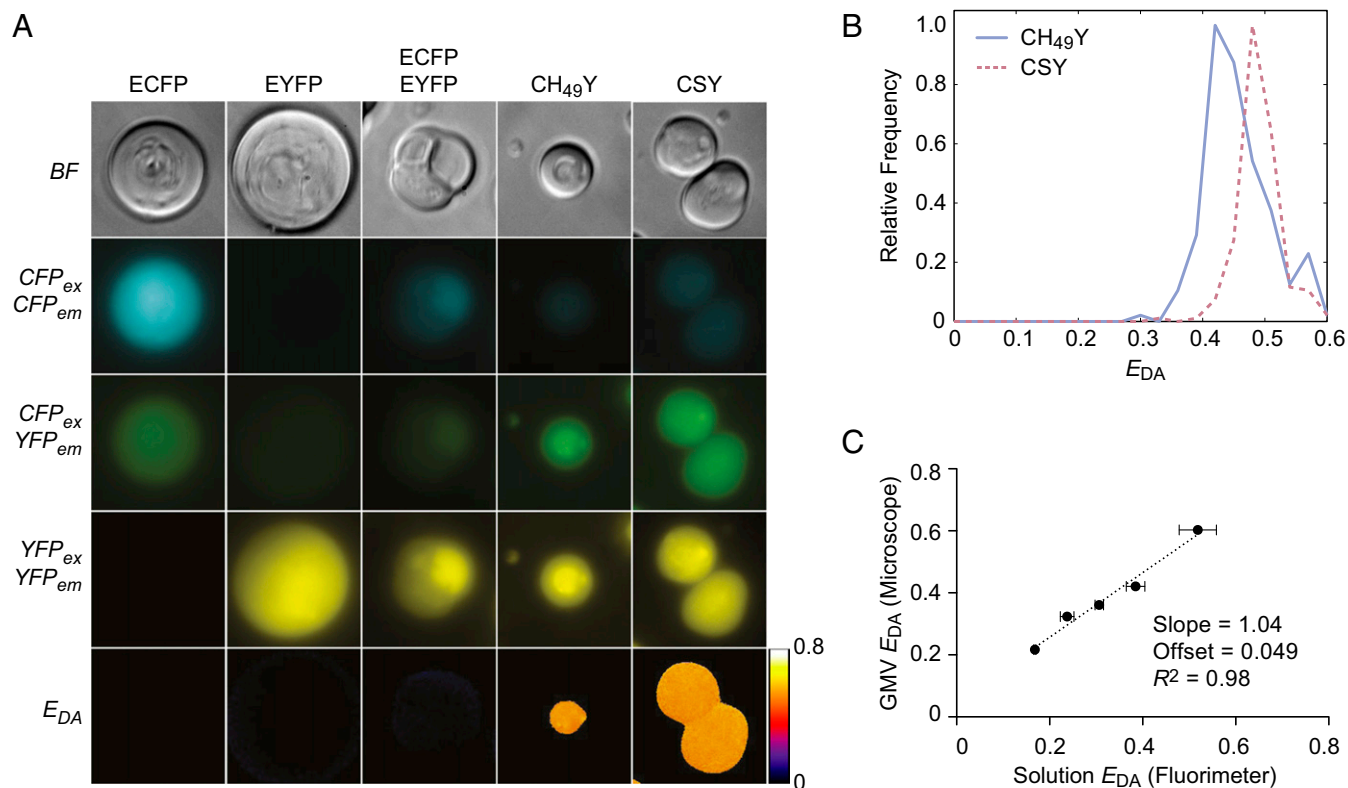


Fig. 3. Encapsulation of sensor protein library into giant multilamellar vesicles (GMVs) to establish correlation between donor–acceptor energy transfer determined by fluorimetry versus microscopy. (A) Representative images of CH₄₉Y, CSY, ECFP, EYFP, and ECFP+EYFP encapsulated in GMVs illustrate relative brightness in each fluorescence channel. (B) Distributions of E_{DA} for GMVs containing apo-CH₄₉Y (blue solid line) and CSY (red dashed line). (C) E_{DA} for the sensor library described in Fig. 2A determined by microscopy are plotted against those determined by fluorimetry. Error bars represent 95% CIs.

question to directly and quantitatively address. Therefore, we sought to use our sensor to specifically quantify changes in the concentration of cytosolic labile heme upon parasite exposure to chloroquine.

We first established that parasites expressing CH₄₉Y and CSY did not show altered sensitivity to chloroquine by determining IC₅₀ values. We determined that both lines had similar chloroquine IC₅₀ values of 10.3–11.3 and 11.4–12.1 nM (95% CIs), respectively, which were comparable to that of the parental NF54^{attB} line (8.2–9.7 nM) (Fig. 5A). These data suggest that CH₄₉Y does not directly interfere with chloroquine action by sequestering heme to prevent potential toxic effects associated with chloroquine-induced increases in labile heme levels. We then exposed highly synchronous ring-stage parasites expressing either CH₄₉Y or CSY to various chloroquine concentrations, and determined cytosolic labile heme concentrations. In four independent experiments, we detected a significant increase in labile heme concentration with 60 nM chloroquine treatment compared with the untreated control (average $\Delta[\text{heme}] = +0.86 \mu\text{M}$; $P = 0.002$) (Fig. 5B and C). Because chloroquine binds heme, it is possible that it competes with our sensor and potentially interferes with accurate measurement of labile heme levels. We evaluated this in vitro by precomplexing 0.5 μM CH₄₉Y and 0.5 μM CSY in parallel with 5 μM heme, titrating chloroquine levels and monitoring apparent changes in measured heme concentrations using normalized E_{DA} calculations as earlier described (Fig. S9). These data show that increasing chloroquine concentrations reduces apparent labile heme levels. However, at stoichiometric or higher chloroquine:heme ratios, apparent labile heme levels detected plateaus at ~50–60% of actual levels even at a 10-fold excess of chloroquine over heme concentrations. This suggests that chloroquine can lead to an underestimation of

labile heme levels by up to ~2.5-fold. Chloroquine, although applied at 60 nM in the media, accumulates over 1,000-fold in the parasite's DV to reach micromolar levels (32). However, the extent with which it “leaks” into the parasite's cytosol in our experiments cannot be easily determined. Nevertheless, using our in vitro data, we can place lower (~2.8 μM) and upper (~7 μM) bounds on labile cytosolic heme levels, assuming, respectively, that no chloroquine or a $\geq 1:1$ ratio of chloroquine:heme is present in the cytosolic compartment.

As a negative control, we treated highly synchronous ring-stage parasites with the antifolate pyrimethamine, which exerts its antimalarial activity by inhibiting DNA synthesis rather than interfering with heme metabolism. No increase in labile heme concentration was detected between the treated and untreated parasites (Fig. 5C), consistent with pyrimethamine's mode of action. Altogether, these data demonstrate that a model heme-interacting antimalarial compound specifically induces a significant increase in cytosolic labile heme that can be quantified using our heme sensor. These data also add biological insight by demonstrating that the increase in cytosolic labile heme is unlikely to be a generalized cytotoxic response, but rather one that is directly and specifically linked to chloroquine-mediated dysregulation of parasite heme homeostasis.

Discussion

Here, we report the development and application of a heme biosensor to measure cytosolic labile heme levels in live, blood-stage *P. falciparum* malarial parasites. Our approach is distinct from some previous strategies used to measure intracellular labile heme in providing the important advantages of obtaining quantitative information from intact cells. Several previous methods have relied on measuring the heme-dependent enzymatic activities

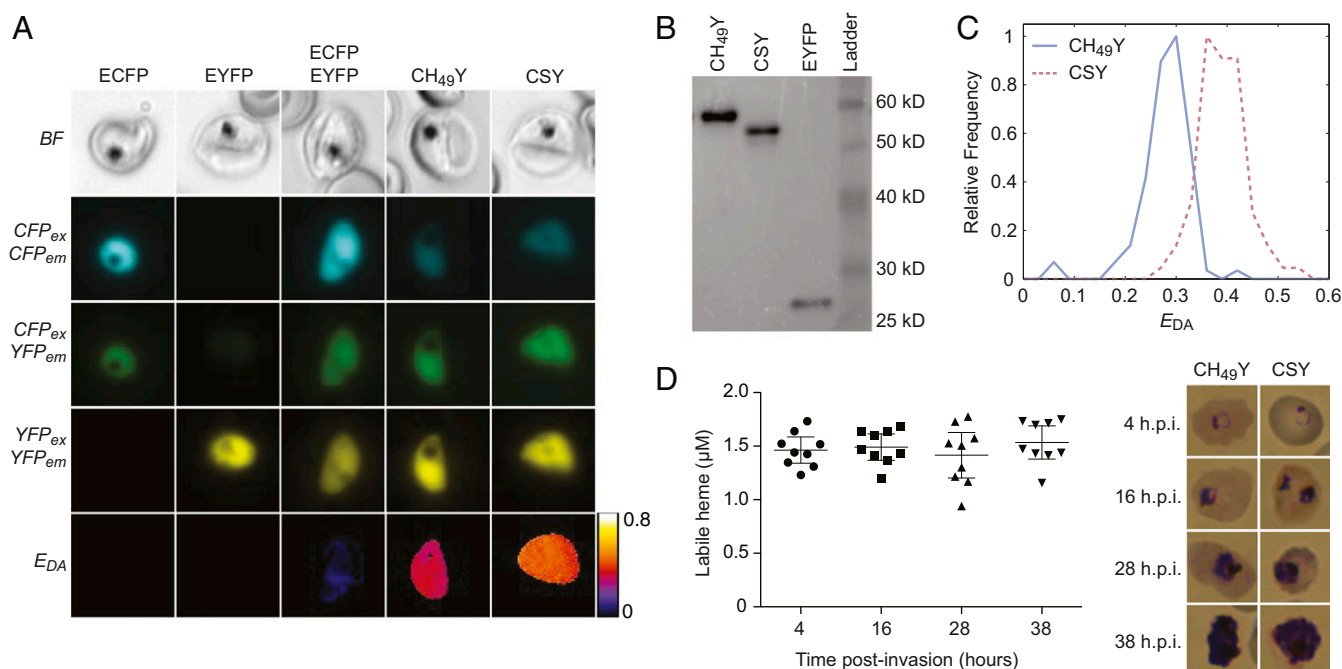


Fig. 4. Using genetically encoded heme sensor to measure cytosolic labile heme concentrations in *P. falciparum*. (A) Representative images of CH₄₉Y, CSY, ECFP, EYFP, and ECFP+EYFP in trophozoite-stage *P. falciparum* parasites. (B) Anti-GFP Western blot of lysates obtained from trophozoite-stage parasites expressing CH₄₉Y, CSY, and YFP. (C) Representative E_{DA} distributions for *P. falciparum* trophozoites expressing CH₄₉Y (solid line) and CSY (dashed line). Using the calibration curve in Fig. 2E yields an average cytosolic labile heme concentration of 1.6 μM (95% CI: 1.56–1.61 μM) across 15 independent experiments. (D) Quantitation of cytosolic labile heme over the *P. falciparum* IDC. Representative images of Giemsa-stained parasites to confirm the parasite stage being analyzed are shown for each time point. Measurements of CH₄₉Y and CSY lines were made in triplicate, resulting in nine ratio calculations as described in *Materials and Methods*. Error bars represent 95% CIs.

of L-tryptophan-2,3-dioxygenase and ALAS (33, 34) natively present in select cell types or recombinantly expressed horseradish peroxidase (HRP) (35). Fractionation methods have also been reported (16, 36). These methods require cell lysis, which makes it difficult to confidently infer the subcellular localization of labile heme. Genetically encoded heme sensors, such as the one we have developed and two recently reported while this study was in progress (37, 38), can facilitate imaging and quantification of heme in different subcellular compartments in intact cells. Therefore, these tools should broadly enable determination of both the distribution and labile heme levels at subcellular and single-cell resolution.

Using our sensor, we show that *P. falciparum* maintains an ~1.6 μM labile cytosolic heme pool throughout its development

in RBCs. It is useful to place this finding in context of previous data on labile heme levels in other organisms and cell types. Several recent reports have used genetically encoded FRET (37), ratiometric fluorescence (38), and hemoprotein peroxidase sensors (39, 40) to measure labile heme in *Saccharomyces cerevisiae* and various mammalian cells. These data show that mean resting labile heme levels ranged from 20 to 40 nM in *S. cerevisiae* (38) and a subset of mammalian cell lines (37) to 433 [95% CI: 186–683 nM (40)] in HEK293 kidney fibroblast cells and 614 nM [95% CI: 183–1,042 nM (39)] in IMR90 lung fibroblast cells. When the medium was supplemented with heme, IMR90 cells accumulated labile heme to a maximum of ~2 μM, suggestive of a threshold regulatory response (39). These data

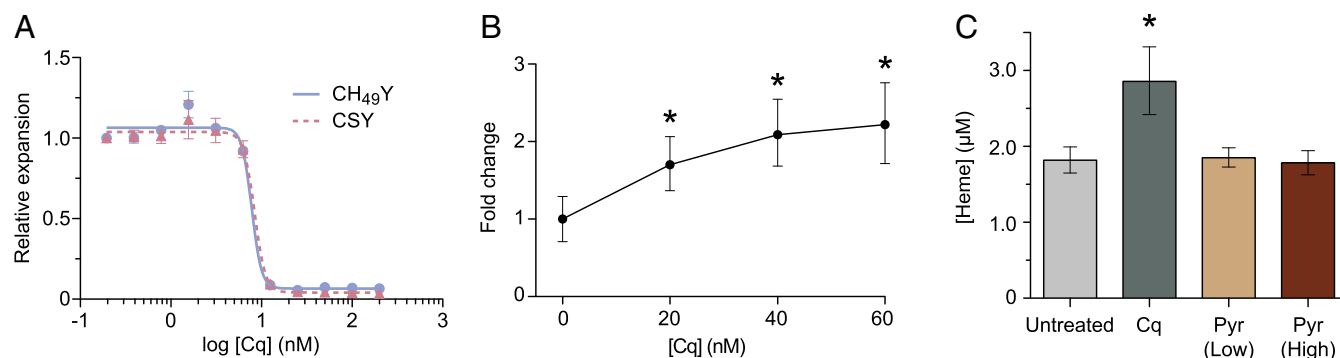


Fig. 5. Quantifying the impact of chloroquine on cytosolic labile heme pool in *P. falciparum*. (A) Growth inhibition data comparing the sensitivity of parasites expressing CH₄₉Y (blue) and CSY (red) to chloroquine. (B) Fold change in labile heme concentration at various chloroquine concentrations after 24-h exposures. Data are representative of three independent experiments. Error bars show 95% CI. (C) Cytosolic labile heme concentrations in parasites that were untreated or exposed to chloroquine (60 nM) or pyrimethamine (125 and 500 nM) for 32 h. Data are representative of three independent experiments. Error bars represent 95% CIs derived from bootstrapping calculations (*Materials and Methods*).

indicate that labile heme levels vary across cell types/organisms, and reach up to 2 μ M. Our measurements in *P. falciparum* extend our understanding of labile heme levels by examining a pathogen with an unusual biology that establishes large heme fluxes through a specialized DV. Between 30 and 70% of the RBC hemoglobin is proteolytically degraded (9, 10) to release heme (\sim 15 mM), which is mostly crystallized to hemozoin. However, our data show that labile cytosolic heme levels—albeit somewhat higher—are reasonably comparable with those reported for HEK293 and IMR90 cells, which likely do not experience similarly large heme fluxes as *P. falciparum*. Altogether, these data reinforce the high efficiency with which hemoglobin-derived heme is confined to the DV, such that labile cytosolic levels remain relatively low and tightly regulated.

The source of heme used by the parasite to maintain this cytosolic pool is unknown, but scavenging from the DV where hemoglobin degradation is occurring, de novo biosynthesis, and uptake from extracellular sources are formal possibilities. Previous qualitative evidence suggests that blood-stage parasites synthesize heme de novo (13, 14), but the extent to which this contributes to the heme pool we measure is unknown. Moreover, recent studies have shown that the parasite's biosynthetic pathway is dispensable during blood-stage development (13, 30), suggesting that biosynthesis may not be a critical source of heme for the parasite during this stage. Developing parasites are also known to become increasingly permeable to extracellular low-molecular-weight solutes via the new permeability pathway (41), so labile heme could potentially be acquired via this route. However, the largest obvious flux of heme in blood-stage parasites is through hemoglobin degradation in the DV. Therefore, this seems to be a reasonable candidate source of heme for the parasite. Additional studies will be needed to definitively and quantitatively address this possibility.

Although the exact source and physiologic role(s) of this labile cytosolic heme pool remain to be defined, our data show that the heme-binding antimalarial drug chloroquine dysregulates this pool. Although chloroquine accumulates to high levels within the DV to interfere with heme crystallization (11), our data quantify the in situ increase in cytosolic heme levels that potentially arises due to heme escaping the DV as qualitatively described previously (16). It is important to emphasize that our sensor likely responds only to the soluble fraction of released heme, and not the fraction that becomes associated with the parasite membrane (42). Thus, our measurements do not reflect the total heme flux induced by chloroquine treatment. This distinction is important, as these two heme pools can potentially induce different outcomes. Membrane-associated heme will likely contribute to cell membrane damage, whereas increased soluble heme could induce cytosolic oxidative stress and/or directly interfere with critical protein function(s) (43). In this model, both heme pools can contribute to cytotoxicity. Alternatively, moderate increases in cytosolic heme may be tolerated without significantly increased toxicity, and increases in soluble heme levels may be directly sensed by the parasite to initiate critical heme-dependent changes in transcription (1, 44, 45), translation, and/or proteasome-mediated protein turnover (46, 47), as in other organisms. These may serve to coordinate changes in DV metabolism with nuclear and cytosolic events that either counteract or exacerbate any adverse effects induced by increased efflux of heme from the DV into the cytoplasm. The responses to increased heme flux induced by antimalarial compounds likely overlap with the mechanisms for maintaining heme homeostasis. Guided by this quantitative understanding of labile heme levels in *P. falciparum*, elucidating these mechanisms can stimulate development of therapeutic strategies that recapitulate important aspects of chloroquine's antimalarial mode(s) of action, while circumventing resistance mechanisms that now limit its effectiveness. Compounds that induce dysregulation of parasite labile heme pools and/or key heme-regulated processes

may be especially promising leads given the extraordinary success of the 4-aminoquinoline antimalarial drug class.

Overall, we have used a genetically encoded heme sensor to examine a long-standing gap in our knowledge of labile heme pools in human malaria parasites. The improved ability to quantify heme in live parasites at subcellular resolution will be useful for gaining insight into how natural perturbations in or deliberate manipulation of labile heme levels contribute, respectively, to heme-dependent signaling and devising antimalarial therapeutic strategies.

Materials and Methods

Molecular Cloning. A fragment of the *P. falciparum* HRP2 gene (109–916 bp) lacking the N-terminal signal peptide was amplified by PCR from plasmid MRA-67 (ATCC/MR4) and cloned into pET28b (Novagen) vectors containing ECFP and EYFP using standard restriction and ligation techniques. To generate sensors based on truncated PfHRP2, a forward oligonucleotide primer was designed to anneal to a repeated PfHRP2 sequence motif identified using MEME (48) and was used with a fixed reverse primer to PCR amplify fragments of varying sizes using the PfHRP2 gene as a template. These were separated by agarose gel electrophoresis, and then cloned into ECFP and EYFP-containing vectors as above. Fragments mapped to full-length PfHRP2, except for some minor in-frame insertion/deletion mutations in the histidine-rich repeats. For CH₁₈Y, the oligonucleotide encoding the heme-binding motif (HHAHHAADA)₂ was generated in a Klenow reaction and cloned as above. For expression in *P. falciparum*, coding sequences from pET28b-based vectors were PCR amplified and cloned using the Gibson Assembly Master Mix (New England Biolabs) to replace the ENR-GFP fusion protein in plasmid MRA-846 (ATCC/MR4).

Protein Expression and Purification. Plasmids encoding sensor and control proteins were transformed into *Escherichia coli* strain BL21(DE3). Cultures were grown overnight at 37 °C in ZYM-505 media (49) supplemented with kanamycin. Saturated cultures were diluted 1:200 in kanamycin-containing ZYM-505 media and grown at 37 °C until OD₆₀₀ = 0.6–0.8. Protein expression was induced by adding 0.1 mM isopropyl β -D-1-thiogalactopyranoside for 24 h at room temperature. Cells were harvested by centrifugation, and pellets were frozen and stored at –80 °C. For protein purification, cell pellets were thawed at room temperature and lysed with B-PER II bacterial protein extraction reagent (Thermo Scientific) supplemented with lysozyme, Benzonase (Novagen), and protease inhibitor mixture (Sigma-Aldrich). Lysates were clarified by centrifugation and applied to purification beads that had been previously washed with Equilibration/Wash Buffer [50 mM Tris-HCl, pH 8.0, 200 mM NaCl, 5% (vol/vol) glycerol]. Hexahistidine-tagged protein constructs were bound to HisPur Cobalt Resin (Thermo Scientific), whereas Strep-Tactin Superflow Plus (Qiagen) was used to bind Strep-tagged proteins. In both cases, lysates were incubated with purification beads for 1 h at 4 °C with gentle agitation. Purification beads were then washed extensively with ice-cold Equilibration/Wash Buffer, before loading on to a gravity-flow column. Hexahistidine-tagged proteins were eluted from the column with Elution Buffer H (50 mM Tris-HCl, pH 8.0, 200 mM NaCl, 500 mM imidazole, 5% glycerol). Strep-tagged proteins were eluted from the column with Elution Buffer S (50 mM Tris-HCl, pH 8.0, 200 mM NaCl, 2.5 mM desthiobiotin, 5% glycerol). Fractions were spectroscopically monitored using a NanoDrop spectrophotometer (Thermo Scientific), and those containing ECFP and/or EYFP were pooled and concentrated using Amicon Ultra-15 centrifugal filters (Thermo Scientific). Concentrated protein solutions were then dialyzed against 2 \times PBS, pH 7.4. Glycerol was then added to 50% and protein solutions were stored at –20 °C.

Absorbance Titrations. Titrations to measure heme-binding affinity and stoichiometry were performed as previously described (19, 23). Stock solutions of recombinant protein were prepared in 100 mM Hepes-KOH, pH 7.0. Stock solutions of 1 mM hemin (Sigma-Aldrich) were prepared in DMSO. All concentrations were verified spectrophotometrically. Heme-binding titrations were performed in 3-mL-capacity quartz cuvettes at 37 °C with stirring using a Cary 100 Bio Spectrophotometer (Varian). Heme titrations were performed with 2 mL of 0.5 μ M protein solution, using 2 mL of Hepes-KOH as a reference. For each concentration, heme was added to both the sample and reference cells and stirred for 5 min before difference spectra were measured. Heme binding was quantified based on a differential absorption peak at 416 nm. The $\Delta A_{416\text{nm}}$ versus heme concentration data were plotted and analyzed using Prism (GraphPad Software).

Fluorescence Titrations and Energy Transfer Efficiency Calculations. Hemin stock solution was serially diluted in Hepes-KOH in a 96-well plate. Protein stock solution was added to 0.5 μ M final concentration using a multichannel pipetter, and the plate was incubated at 37 °C for 5 min. Fluorescence spectra were measured using a Fluoromax-3 fluorimeter (Horiba Jobin Yvon). ECFP was excited at 420 nm, with emission scanning from 440 to 600 nm. EYFP was excited at 500 nm, with emission scanning from 505 to 600 nm. Energy transfer efficiencies were calculated using the ratio_A method as previously described (6, 27).

Fluorescence Lifetime Spectroscopy. The multiphoton FLIM microscope consisted of a Ti:sapphire laser (Tsunami HP; Spectra Physics), tunable between 780 and 880 nm (Fig. S2). Power control was achieved using a half waveplate and Glan-Laser polarizer. The beam first struck a tilted glass coverslip beam splitter where part of the beam was focused onto a photodiode to create a reference pulse. The majority of the pulse intensity passed through the beam splitter to the rest of the microscope. The beam was subsequently reflected off a dichroic beam splitter (675DCSX; Chroma Technology) and two galvanometric scanning mirrors (6350; Cambridge Technology) before entering the scan lens, which produced a moving focal spot at the image plane of the microscope (Axiovert 100TV; Zeiss). The scanning mirrors were controlled using software written in-house, and the synchronization signals were created using an FPGA (Spartan XCS30; Xilinx).

The spot in the image plane was imaged onto the sample by the microscope objective (C-Apochromat, 40 \times , water immersion; 44-00-52; Zeiss), and the resulting fluorescence emission was captured by the objective, descanned by the scanning mirrors, and passed through the dichroic mirror and filter (ESP650; Chroma Technology), where it was focused onto a photomultiplier tube (R7400P; Hamamatsu). The signal from the photomultiplier and the signal from the reference photodiode were measured by a Time-Correlated Single Photon Counting Card (SPC-730; Becker and Hickl), and the resulting image was displayed using the Becker and Hickl software.

The instrument response was compensated for by measuring a sample (fluorescein in pH 9 DMSO solution, from R14782 reference sample kit; Life Technologies; known lifetime of 4.1 ns) and deconvolving the known decay curve from the measured curve to yield the instrument response. This instrument response was then deconvolved from every measured curve to yield a corrected decay curve. After this correction, the exponentially decaying section of the curve was taken from the data, and a "single exponential decay with unknown offset" function was fitted to the data to recover the fluorescence lifetime while compensating for the small background in the measurement. All calculations were performed using MATLAB 2011b (MathWorks).

Malaria Parasite Culture. Blood-stage malaria parasites were cultured at 2% hematocrit in 5% O₂ and 5% CO₂ in RPMI medium 1640 supplemented with 5 g/L AlbumAX II (Life Technologies), 2 g/L NaHCO₃, 25 mM Hepes-KOH, pH 7.4, 1 mM hypoxanthine, and 50 mg/L gentamicin. Strains were synchronized using a solution of 0.3 M alanine supplemented with 25 mM Hepes-KOH, pH 7.4. Parasite transfections were performed by preloading RBCs with plasmid DNA by electroporation. All expression constructs were integrated at the *cg6* locus in NF54^{attB} parasites (29) by cotransfecting with the pINT plasmid (MRA-847) (50). For each transfection, 100 μ L of washed RBCs was mixed with 25–50 μ g of plasmid DNA and then electroporated with 8 \times 1-ms square pulses at 365 V. Late-stage parasites were then split to 0.1% parasitemia using one-half of the loaded RBCs. After 48 h, transfected cultures were split 1:2 using the remainder of the loaded RBCs. After another 48 h, cultures were split again, and drug selection was initiated. Drug-resistant parasites were then cloned by limiting dilution, and clones were screened for expression of ECFP and/or EYFP using flow cytometry.

Preparation of GMVs. Stock solutions of 1,2-dioleoyl-*sn*-glycero-3-phospho-(1'-*rac*-glycerol) (DOPG) and 1,2-dioleoyl-*sn*-glycero-3-phosphocholine (DOPC) (Avanti Polar Lipids) in chloroform were mixed in a 1:1 ratio, and 1 μ mol of total lipid was added to a glass scintillation vial. Lipid films were deposited by overnight evaporation of the chloroform at room temperature. Lipid films were then hydrated by incubating scintillation vials in a humidified 70 °C oven for 6 h. Vesicles were prepared by gently adding protein solutions (0.5 μ M protein in 100 mM Hepes-KOH, pH 7, plus 50 mM sucrose) and incubating overnight at room temperature in the dark. After

incubation, vesicles were washed extensively in Hepes-KOH plus 50 mM glucose and imaged.

In Situ Analysis of Donor–Acceptor Energy Transfer. Synchronized late-stage parasite cultures were washed and resuspended in Opti-Klear media (Marker Gene Technologies) at 0.05% hematocrit for imaging. Culture suspensions were added to glass-bottom 24-well plates (In Vitro Scientific) pretreated with 0.1% polyethyleneimine. Cultures were imaged using a Nikon Ti microscope using the following filter sets: ECFP [436 nm/20 nm excitation (EX), 455 nm long pass (LP), 480 nm/40 nm emission (EM)], FRET (436 nm/20 nm EX, 455 nm LP, 535 nm/30 nm EM), and YFP (500 nm/20 nm EX, 515 nm LP, 535 nm/30 nm EM). Images were acquired using an Andor iXon+ 897 EMCCD camera and MetaMorph acquisition software (Molecular Devices). Images were processed using Biosensor Processing Software, version 2.1 (51). Briefly, images were shade-corrected using averaged reference images, and segmentation values were chosen for each channel by manual inspection to draw background masks, which were then grown using a 5-pixel radius. Background subtraction was performed according to software defaults. The FRET channel was corrected for bleedthrough from CFP and cross talk from YFP using correction factors of 0.4 and 0.1, respectively. Images were obtained by calculating the ratio between the corrected FRET channel image and the YFP image, and manually curated to identify individual cells. Average per-cell E_{DA} for CH₄₉Y and CSY strains were calculated and tabulated using the FIJI distribution of ImageJ (52). A bootstrapping algorithm with 10,000 iterations was used to estimate the ratio of averages between CH₄₉Y and CSY energy transfer distributions, correct for the offset measured between microscopy and fluorimetry data, and compute a 95% CI. The ratio of averages and the CI bounds were used to calculate heme concentrations according to the following empirically determined relationship between normalized E_{DA}^{CH49Y} and heme (Fig. 2 D and E):

$$\text{Normalized } E_{DA}^{\text{Sensor}} = \frac{E_{DA, \text{CH49Y}}}{E_{DA, \text{CSY}}} = \frac{0.41e^{-0.18[\text{Heme}]} - 0.027}{0.41 - 0.01[\text{Heme}]}$$

Calculations were performed using MATLAB R2013a software (MathWorks).

Western Immunoblotting. Parasites were obtained by lysing 180 μ L of infected RBCs with an ice-cold solution of 0.1% saponin (Fluka) in PBS and incubating on ice until solutions cleared. Parasite pellets were washed extensively with saponin–PBS solution to remove residual hemoglobin and then lysed with the addition of 200 μ L of 1 \times SDS–urea sample buffer (40 mM Tris base, 80 mM Gly–Gly, 40 mM DTT, 1.6% SDS, and 6.4 M urea adjusted to pH 6.8 with HCl). Parasite lysates were diluted 1:10 before gel electrophoresis and transfer. Blots were probed with a mouse monoclonal anti-GFP (B-2) primary antibody (catalog no. SC-9996; Santa Cruz Biotechnology) diluted 1:2,000, and a goat anti-mouse secondary antibody conjugated to HRP (H+L) (catalog no. 71045; Novagen), and visualized using SuperSignal West Femto chemiluminescent substrate (Thermo Scientific).

ACKNOWLEDGMENTS. We thank Wendy Salmon, Glenn Paradis, Prabhani Akutrale, and Ceth Parker for technical assistance. We also thank Hunter Elliott and Matthew Edwards for valuable feedback. The following reagents were obtained through the MR4 as part of the Biodefense and Emerging Infections Research Resources Repository, National Institute of Allergy and Infectious Diseases, NIH: *Plasmodium falciparum* HRP1 expression vector (MRA-67; deposited by D. E. Goldberg), pLN-ENR-GFP (MRA-846; deposited by D. A. Fidock), and pINT (MRA-847; deposited by D. A. Fidock). Flow cytometry was performed in the Genomics and Imaging Facilities Core of the Massachusetts Institute of Technology (MIT) Center for Environmental and Health Sciences (supported by National Institute of Environmental Health Sciences Center Grant P30-ES002109) and Flow Cytometry Core at the Koch Institute for Integrative Cancer Research at MIT. This work was supported by National Institute of General Medical Sciences (NIGMS) Biotechnology Training Grant 5-T32-GM08334 (to J.R.A.), NIH Director's New Innovator Award 1DP2OD007124 (to J.C.N.), NIGMS Center for Integrative Synthetic Biology Grant P50-GM098792, Ferry Award (to J.C.N.), and MIT startup funds (to J.C.N.). P.T.C.S. acknowledges support from NIH Grants 5-P41-EB015871-27, DP3-DK101024 01, 1-U01-NS090438-01, 1-R01-EY017656-06A1, and 1-R01-HL121386-01A1; the Singapore-MIT Alliance 2; the BioSystems and Micromechanics Interdisciplinary Research Group of Singapore-MIT Alliance Research and Technology Center and the MIT SkolTech Initiative; and the Koch Institute for Integrative Cancer Research Bridge Initiative. C.J.R. is grateful for a Wellcome Trust MIT Postdoctoral Research Fellowship to carry out this research. This work was supported by the Wellcome Trust.

- Girvan HM, Munro AW (2013) Heme sensor proteins. *J Biol Chem* 288(19):13194–13203.
- Poulos TL (2014) Heme enzyme structure and function. *Chem Rev* 114(7):3919–3962.
- Khan AA, Quigley JG (2011) Control of intracellular heme levels: Heme transporters and heme oxygenases. *Biochim Biophys Acta* 1813(5):668–682.

- Ziegler J, Linck R, Wright DW (2001) Heme aggregation inhibitors: Antimalarial drugs targeting an essential biomineralization process. *Curr Med Chem* 8(2):171–189.
- Pluth MD, Tomat E, Lippard SJ (2011) Biochemistry of mobile zinc and nitric oxide revealed by fluorescent sensors. *Annu Rev Biochem* 80:333–355.

6. Kolosov VL, et al. (2008) Engineering redox-sensitive linkers for genetically encoded FRET-based biosensors. *Exp Biol Med* (Maywood) 233(2):238–248.
7. WHO (2015) *World Malaria Report: 2015* (World Health Organization, Geneva).
8. Egan TJ, et al. (2002) Fate of haem iron in the malaria parasite *Plasmodium falciparum*. *Biochem J* 365(Pt 2):343–347.
9. Esposito A, et al. (2008) FRET imaging of hemoglobin concentration in *Plasmodium falciparum*-infected red cells. *PLoS One* 3(11):e3780.
10. Hanssen E, et al. (2012) Soft X-ray microscopy analysis of cell volume and hemoglobin content in erythrocytes infected with asexual and sexual stages of *Plasmodium falciparum*. *J Struct Biol* 177(2):224–232.
11. Sigala PA, Goldberg DE (2014) The peculiarities and paradoxes of *Plasmodium* heme metabolism. *Annu Rev Microbiol* 68:259–278.
12. Gardner MJ, et al. (2002) Genome sequence of the human malaria parasite *Plasmodium falciparum*. *Nature* 419(6906):498–511.
13. Nagaraj VA, et al. (2013) Malaria parasite-synthesized heme is essential in the mosquito and liver stages and complements host heme in the blood stages of infection. *PLoS Pathog* 9(8):e1003522.
14. Surolija N, Padmanaban G (1992) De novo biosynthesis of heme offers a new chemotherapeutic target in the human malarial parasite. *Biochem Biophys Res Commun* 187(2):744–750.
15. Arie F, et al. (2014) A molecular marker of artemisinin-resistant *Plasmodium falciparum* malaria. *Nature* 505(7481):50–55.
16. Combrinck JM, et al. (2013) Insights into the role of heme in the mechanism of action of antimalarials. *ACS Chem Biol* 8(1):133–137.
17. Atamna H, Ginsburg H (1995) Heme degradation in the presence of glutathione. A proposed mechanism to account for the high levels of non-heme iron found in the membranes of hemoglobinopathic red blood cells. *J Biol Chem* 270(42):24876–24883.
18. Okumoto S, Jones A, Frommer WB (2012) Quantitative imaging with fluorescent biosensors. *Annu Rev Plant Biol* 63(1):663–706.
19. Schneider EL, Marletta MA (2005) Heme binding to the histidine-rich protein II from *Plasmodium falciparum*. *Biochemistry* 44(3):979–986.
20. Sullivan DJ, Jr, Gluzman IY, Goldberg DE (1996) *Plasmodium* hemozoin formation mediated by histidine-rich proteins. *Science* 271(5246):219–222.
21. Akompong T, et al. (2002) Trans expression of a *Plasmodium falciparum* histidine-rich protein II (HRPII) reveals sorting of soluble proteins in the periphery of the host erythrocyte and disrupts transport to the malarial food vacuole. *J Biol Chem* 277(32):28923–28933.
22. Evers TH, van Dongen EMWM, Faesen AC, Meijer EW, Merks M (2006) Quantitative understanding of the energy transfer between fluorescent proteins connected via flexible peptide linkers. *Biochemistry* 45(44):13183–13192.
23. Choi CY, Cerdá JF, Chu HA, Babcock GT, Marletta MA (1999) Spectroscopic characterization of the heme-binding sites in *Plasmodium falciparum* histidine-rich protein 2. *Biochemistry* 38(51):16916–16924.
24. Takeda S, Kamiya N, Arai R, Nagamune T (2001) Design of an artificial light-harvesting unit by protein engineering: Cytochrome *b*₅₆₂-green fluorescent protein chimera. *Biochem Biophys Res Commun* 289(1):299–304.
25. Pandey AV, Joshi R, Tekwani BL, Singh RL, Chauhan VS (1997) Synthetic peptides corresponding to a repetitive sequence of malarial histidine rich protein bind haem and inhibit haemozoin formation *in vitro*. *Mol Biochem Parasitol* 90(1):281–287.
26. Ziegler J, Chang RT, Wright DW (1999) Multiple-antigenic peptides of histidine-rich protein II of *Plasmodium falciparum*: Dendritic biomimetic templates. *J Am Chem Soc* 121(11):2395–2400.
27. Clegg RM (1992) Fluorescence resonance energy transfer and nucleic acids. *Methods Enzymol* 211:353–388.
28. Wachter RM, Yarbrough D, Kallio K, Remington SJ (2000) Crystallographic and energetic analysis of binding of selected anions to the yellow variants of green fluorescent protein. *J Mol Biol* 301(1):157–171.
29. Adjalley SH, et al. (2011) Quantitative assessment of *Plasmodium falciparum* sexual development reveals potent transmission-blocking activity by methylene blue. *Proc Natl Acad Sci USA* 108(47):E1214–E1223.
30. Ke H, et al. (2014) The heme biosynthesis pathway is essential for *Plasmodium falciparum* development in mosquito stage but not in blood stages. *J Biol Chem* 289(50):34827–34837.
31. Sidhu ABS, Verdier-Pinard D, Fidock DA (2002) Chloroquine resistance in *Plasmodium falciparum* malaria parasites conferred by *pfcr* mutations. *Science* 298(5591):210–213.
32. Bray PG, et al. (1999) Cellular uptake of chloroquine is dependent on binding to ferriprotoporphyrin IX and is independent of NHE activity in *Plasmodium falciparum*. *J Cell Biol* 145(2):363–376.
33. Granick S, Sinclair P, Sassa S, Grieninger G (1975) Effects by heme, insulin, and serum albumin on heme and protein synthesis in chick embryo liver cells cultured in a chemically defined medium, and a spectrofluorometric assay for porphyrin composition. *J Biol Chem* 250(24):9215–9225.
34. Lincoln BC, Alvarado A, Setty N, Bonkovsky HL (1988) Tryptophan 2,3-dioxygenase in chick embryo hepatocytes: Studies *in ovo* and in culture. *Proc Soc Exp Biol Med* 188(3):308–315.
35. White C, et al. (2013) HRG1 is essential for heme transport from the phagolysosome of macrophages during erythrophagocytosis. *Cell Metab* 17(2):261–270.
36. Liu SC, Zhai S, Palek J (1988) Detection of heme release during hemoglobin S denaturation. *Blood* 71(6):1755–1758.
37. Song Y, et al. (2015) A genetically encoded FRET sensor for intracellular heme. *ACS Chem Biol* 10(7):1610–1615.
38. Hanna DA, et al. (2016) Heme dynamics and trafficking factors revealed by genetically encoded fluorescent heme sensors. *Proc Natl Acad Sci USA* 113(27):7539–7544.
39. Atamna H, Brahmabhatt M, Atamna W, Shanower GA, Dhahbi JM (2015) ApoHRP-based assay to measure intracellular regulatory heme. *Metalomics* 7(2):309–321.
40. Yuan X, et al. (2016) Regulation of intracellular heme trafficking revealed by subcellular reporters. *Proc Natl Acad Sci USA* 113(35):E5144–E5152.
41. Martin RE, Ginsburg H, Kirk K (2009) Membrane transport proteins of the malaria parasite. *Mol Microbiol* 74(3):519–528.
42. Ginsburg H, Famin O, Zhang J, Krugliak M (1998) Inhibition of glutathione-dependent degradation of heme by chloroquine and amodiaquine as a possible basis for their antimalarial mode of action. *Biochem Pharmacol* 56(10):1305–1313.
43. Radfar A, Diez A, Bautista JM (2008) Chloroquine mediates specific proteome oxidative damage across the erythrocytic cycle of resistant *Plasmodium falciparum*. *Free Radic Biol Med* 44(12):2034–2042.
44. Ogawa K, et al. (2001) Heme mediates derepression of Maf recognition element through direct binding to transcription repressor Bach1. *EMBO J* 20(11):2835–2843.
45. Smart JL, Bauer CE (2006) Tetrapyrrole biosynthesis in *Rhodospirillum rubrum* is transcriptionally regulated by the heme-binding regulatory protein, HbL. *J Bacteriol* 188(4):1567–1576.
46. Hu R-G, Wang H, Xia Z, Varshavsky A (2008) The N-end rule pathway is a sensor of heme. *Proc Natl Acad Sci USA* 105(1):76–81.
47. Yang F, Xia X, Lei H-Y, Wang E-D (2010) Hemin binds to human cytoplasmic arginyl-tRNA synthetase and inhibits its catalytic activity. *J Biol Chem* 285(50):39437–39446.
48. Bailey TL, Elkan C (1994) Fitting a mixture model by expectation maximization to discover motifs in biopolymers. *Proc Int Conf Intell Syst Mol Biol* 2:28–36.
49. Studier FW (2005) Protein production by auto-induction in high density shaking cultures. *Protein Expr Purif* 41(1):207–234.
50. Nkrumah LJ, et al. (2006) Efficient site-specific integration in *Plasmodium falciparum* chromosomes mediated by mycobacteriophage Bxb1 integrase. *Nat Methods* 3(8):615–621.
51. Hodgson L, Shen F, Hahn K (2010) Biosensors for characterizing the dynamics of rho family GTPases in living cells. *Curr Protoc Cell Biol* Chapter 14:Unit 14.11.1–26.
52. Schindelin J, et al. (2012) Fiji: An open-source platform for biological-image analysis. *Nat Methods* 9(7):676–682.